# Evolution of Titanium Arc Weldment Macro and Microstructures — Modeling and Real Time Mapping of Phases

*Rigorous heat transfer modeling and real-time experimental mapping of phases are used to understand HAZ phase transformations and three-dimensional grain structure evolution during welding*

BY Z. YANG, J. W. ELMER, J. WONG AND T. DEBROY

ABSTRACT. Macro and microstructural features in gas tungsten arc (GTA) welded titanium were modeled for the first time based on a combination of transport phenomena and phase transformation theory. A transient, three-dimensional, turbulent heat transfer and fluid flow model was developed to calculate the temperature and velocity fields, thermal cycles, and the shape and size of the fusion zone. The kinetics of the $\alpha \rightarrow \beta$ allotropic transformation during continuous heating and the corresponding $(\alpha+\beta)/\beta$ phase boundary were calculated using a modified Johnson-Mehl-Avrami (JMA) equation and the calculated thermal cycles. The modeling results were compared with the real-time phase mapping data obtained using a unique spatially resolved X-ray diffraction technique with synchrotron radiation. The real-time evolution of grain structure within the entire weld heat-affected zone (HAZ) was modeled in three dimensions using a Monte Carlo technique.

The following are the major findings. First, the rates of heat transfer and fluid flow in the titanium weld pool during gas tungsten arc welding (GTAW) are significantly enhanced by turbulence, and previous calculations of laminar fluid flow and heat transfer in arc-melted pools need to be re-examined. The fusion zone geometry, and the $\alpha/(\alpha+\beta)$ and $(\alpha+\beta)/\beta$ phase boundaries in the HAZ could be satisfactorily predicted. Second, comparison of real-time $\alpha \rightarrow \beta$ transformation kinetics with the rates computed assuming various alternative reaction mechanisms indicates the transition was most likely controlled by the transport of Ti atoms across the $\alpha/\beta$ interface. Third, comparison of the experimental data with the simulated results indicates the real-time evolution of the grain structure around the weld pool could be simulated by the Monte Carlo technique. Finally, the insight developed in this research could not have been achieved without concomitant modeling and experiments.

*Z. YANG, and T. DEBROY are with Department of Materials Science and Engineering, The Pennsylvania State University, University Park, Pa. J. W. ELMER and J. WONG are with Chemistry and Materials Science Department, Lawrence Livermore National Laboratory, Livermore, Calif.*

## Introduction

The integrity and performance of the weldment depends on both its macro and microstructures. During fusion welding, the interaction of the heat source and the material leads to rapid heating, melting and vigorous circulation of the molten metal in the weld pool. In the weld pool, the heat transfer and fluid flow affect temperature fields and thermal cycles, which, in turn, affect the macro and microstructures of the weld metal. In the solid region around the weld pool, the thermal cycles may lead to solid state phase transformations and changes in the grain structure through annealing, recrystallization and grain growth. The kinetics of the phase transformations and the grain growth vary across the weldment and are functions of both the heating and cooling rates and the maximum temperatures attained during the thermal cycles. These welding-induced spatial variations of microstructures significantly affect the weldment properties such as strength, ductility, toughness and corrosion resistance. Thus, control of the macro and microstructure is important in achieving structurally sound and reliable welds during arc welding.

Knowledge of the thermal cycles in the fusion zone (FZ) and HAZ is a prerequisite for understanding microstructural evolution in the weldment. Accurate measurements of temperature profiles in the FZ and HAZ are difficult, and noncontact techniques for the measurement of surface temperatures are still evolving. Mathematical modeling provides a recourse to overcome the difficulties encountered in temperature measurements. In recent years, modeling of fluid flow and heat transfer in the weld pool have provided detailed insight about the welding processes that could not have otherwise been obtained (Refs. 1–16). Significant progress has been made to understand the development of weld pool shape and size (Refs. 1–6), cooling rate (Ref. 7) and the concentration of volatile alloying elements from the weld pool (Refs. 8, 9). However, ef-

KEY WORDS

GTAW
Titanium
3-D Model
Heat Transfer
Fluid Flow
Phase Mapping
X-ray Diffraction
Grain Growth
Monte Carlo

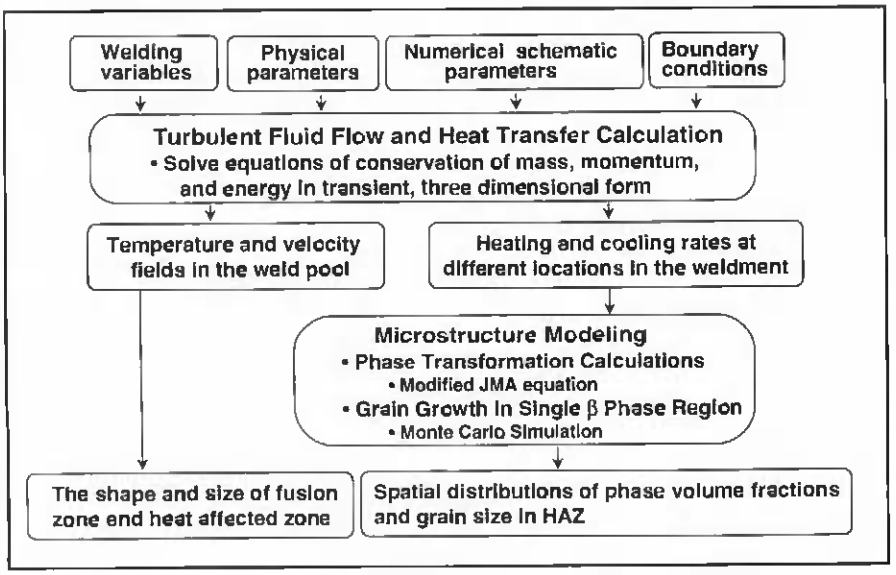


*Fig. — 1 Flow chart.*

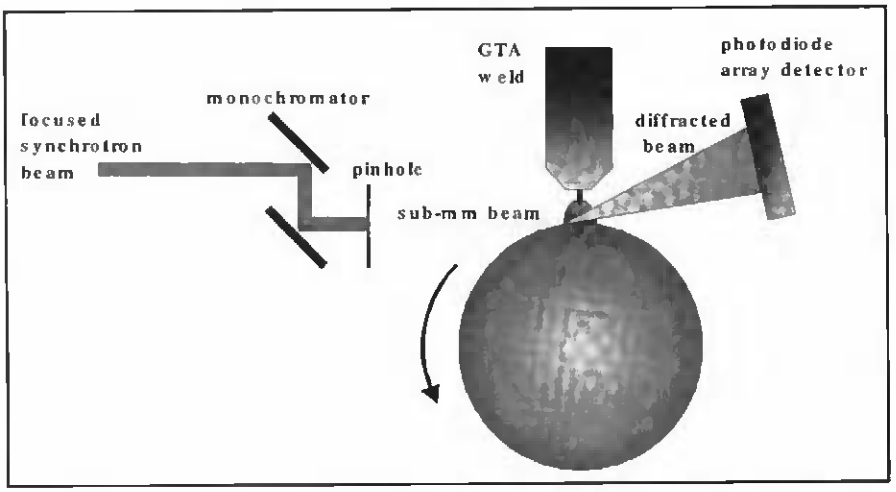


*Fig. 2 — Experimental setup.*

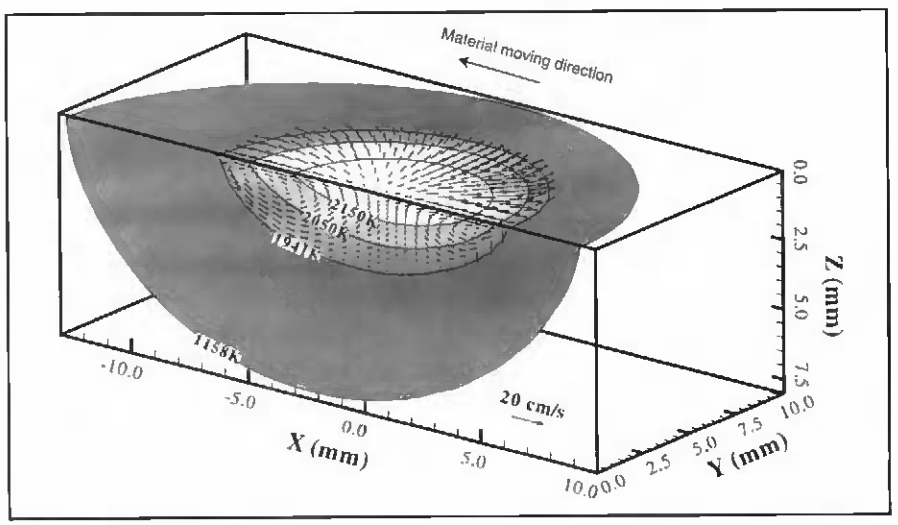


*Fig. 3 — Calculated temperature and velocity fields in three dimensions. Welding conditions: GTA, 100 A, 19 V, 1.1 mm/s welding speed.*

forts to quantitatively model the development of weldment microstructures (Refs. 10–12 ), inclusion characteristics (Ref. 13) and concentrations of dissolved gases in the weld metal (Refs. 14–16) starting from transport phenomena are just beginning.

Accurate calculation of the geometry and the thermal cycles in the weldment requires a well-tested numerical thermofluid model. In the past decade, several numerical thermofluid models (Refs. 1–5) have been established to study heat transfer and fluid flow in arc welding processes in which laminar flow was assumed in the weld pool. However, recent experimental observations (Ref. 17) and theoretical calculations (Refs. 18, 19) in GTA welding have indicated that, in many cases, the fluid flow in the weld pool is turbulent in nature. Previous results from two-dimensional (2-D) calculations strongly suggested that accurate predictions of flow patterns and weld pool geometries will only be possible if the effects of turbulence are modeled accurately (Refs. 18, 19). In the present study, a well-tested, three-dimensional, turbulent heat transfer and fluid flow model (Ref. 12) was used to calculate the temperature field, geometry of the FZ and the thermal cycles in the titanium weldment during GTA welding.

During welding commercially pure titanium, a series of phase transformations take place in both the FZ and the HAZ. The microstructural history of the FZ is $\alpha \rightarrow \beta \rightarrow$liquid$\rightarrow \beta \rightarrow \alpha$, while that of the HAZ is $\alpha \rightarrow \beta \rightarrow \alpha$ (Ref. 20), where $\alpha$ is the hexagonal close-packed form of titanium and $\beta$ is the body-centered-cubic form of titanium. In the present research, both real-time-based experiments and mathematical modeling were used to study the microstructural evolution in the HAZ of titanium weldment. An experimental method (Refs. 20–23) for observing phase transformation behavior during welding using spatially resolved X-ray diffraction (SRXRD) with synchrotron radiation was used to study the phase transformations in real time during the welding of commercially pure titanium. Also, the extents of the phase transitions at various locations were computed by the combination of the calculated thermal cycles and phase transition kinetics.

As a first effort to model the phase transitions in titanium, only the $\alpha \rightarrow \beta$ transition during heating was considered in the present paper because of the uniqueness of the kinetic data that can be obtained from the SRXRD technique. These kinetic data are very difficult to obtain by traditional methods because the microstructures that form during heating are subsequently altered by the transfor-

mations that take place during cooling. Under the present welding conditions, it is believed the α→β transformation in titanium takes place by classical nucleation and growth process rather than martensitic transformation (Ref. 20). Thus, a modified Johnson-Mehl-Avrami (JMA) equation (Ref. 24) was used to calculate the kinetics of the α→β transformation during continuous heating. The degree of the α→β transition and consequently the change of phase concentration at various locations can be calculated by incorporating the calculated thermal cycles into the modified JMA equation. The quantitatively calculated phase distribution combined with the real-time experimental results can help us identify the possible mechanism of the α→β transition during welding.

In addition to the spatial distribution of phases, another important microstructural feature in the HAZ is the significant grain-size gradient. In the past decade, the Monte Carlo (MC) technique has been widely used to simulate the evolution of grain structure under isothermal conditions (Refs. 25–27). Compared with the analytical method (Ref. 30), the Monte Carlo simulation of grain growth can provide not only grain growth kinetics but also detailed information on temporal grain morphology evolution. More recently, the Monte Carlo technique has been used to simulate grain growth in the HAZ of welds (Refs. 28, 29) The simulation of grain growth in the HAZ by the MC technique is more realistic than by the classical analytical equation, because the temperature gradient near the weld interface is steep and the atomic mobility can vary across a single grain. This phenomenon cannot be taken into account by the classical analytical equation; however, it can be effectively simu-

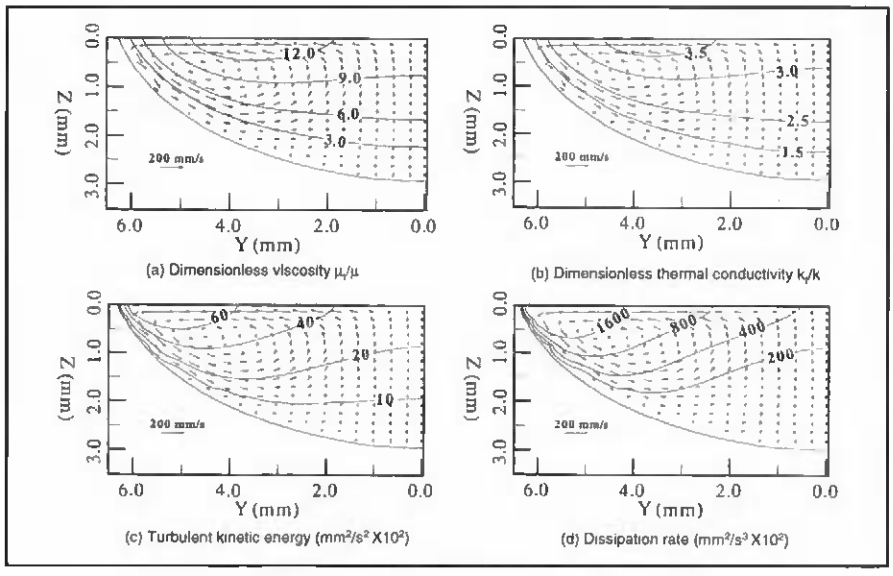


*Fig. 4 — Spatial distribution of turbulent variables.*

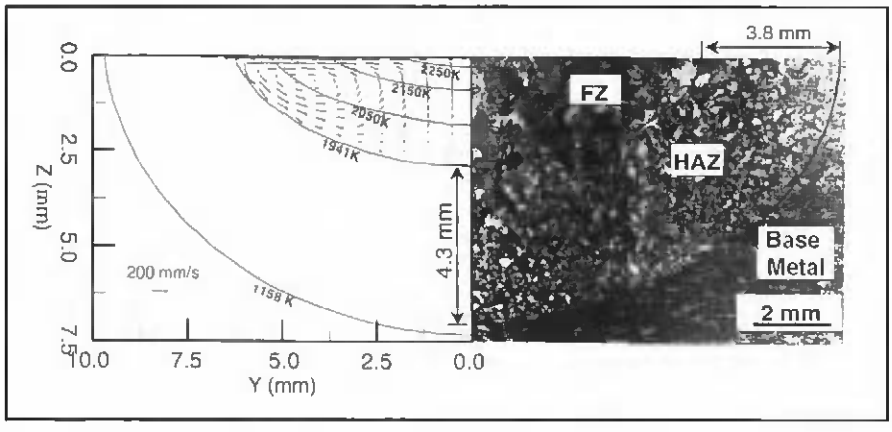


*Fig. 5 — Comparison of the calculated (at location x = 0) and experimental geometries of the FZ and HAZ. The width of the HAZ varies with location. The width of the HAZ on the top surface is less than that at the bottom of the HAZ.*

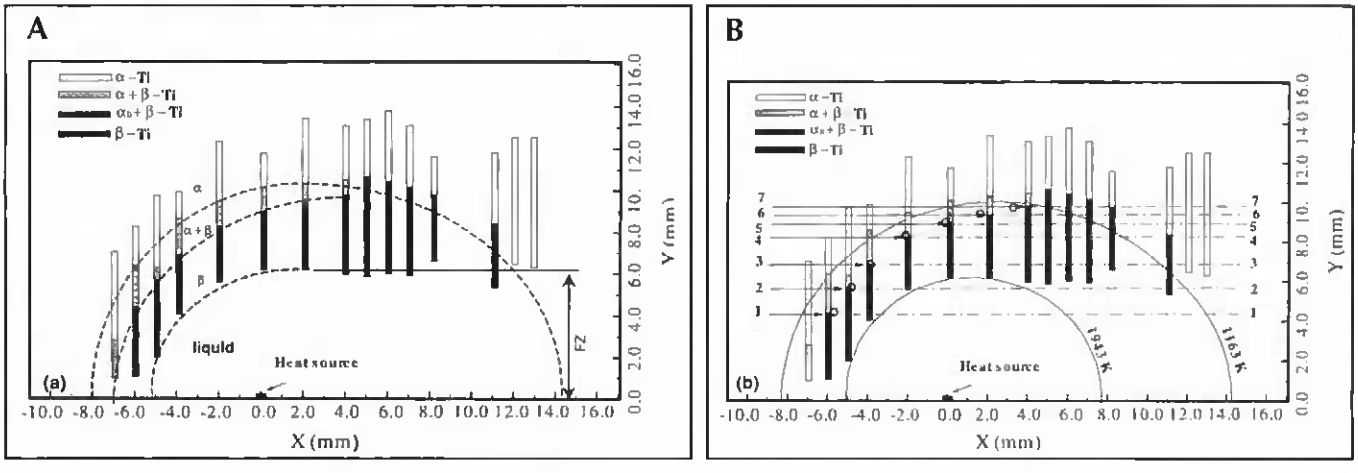


*Fig. 6 — A — Real-time phase distribution map from SRXRD data; B — calculated phase transition isotherms on the phase distribution map. Distances from weld centerline: 1, 4.2 mm; 2, 5.8 mm; 3, 6.6 mm; 4, 8.2 mm; 5, 8.8 mm; 6, 9.2 mm; 7, 9.6 mm.*

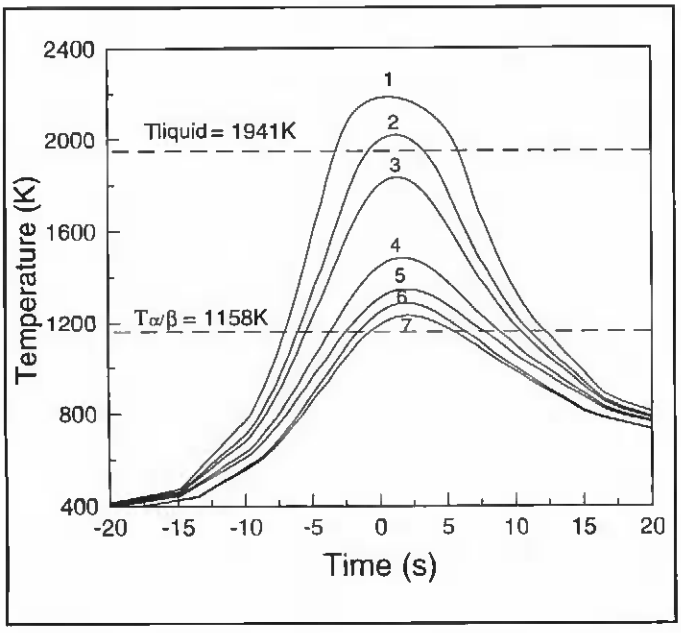


*Fig. 7 — Calculated thermal cycles at different locations. Distances from welding centerline: 1, 4.2 mm; 2, 5.8 mm; 3, 6.6 mm; 4, 8.2 mm; 5, 8.8 mm; 6, 9.2 mm; 7, 9.6 mm.*

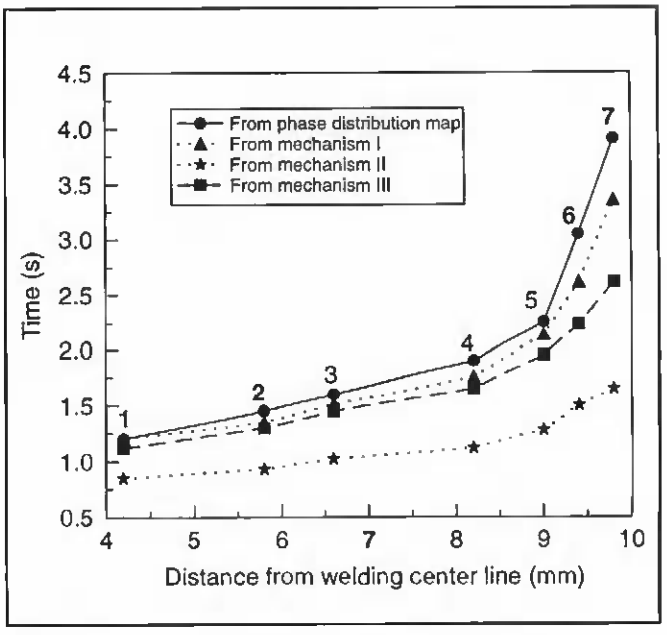


*Fig. 8 — Comparison of the times needed for α→β transformation from JMA equation and from phase distribution map. Different mechanisms assumed for the application of JMA equations are given in Table 2. Distances from weld centerline: 1, 4.2 mm; 2, 5.8 mm; 3, 6.6 mm; 4, 8.2 mm; 5, 8.8 mm; 6, 9.2 mm; 7, 9.6 mm.*

lated by the MC technique, in which the grains are subdivided into many discrete small units and each unit can have its own atomic mobility depending on the local temperature.

Previous simulations of the grain growth in the HAZ were limited to two-dimensional calculations. Considering the significant local thermal and topological environment change in the HAZ, simulation of grain growth in two dimensions is not sufficient for grain growth occurring in real welds that are three dimensional. Furthermore, the width of the HAZ usually varies with the location in the actual weldment. This temperature dependence of spatial dimension variation was ignored in the previous two-dimensional simulations. For more realistic simulation, the purpose of the present investigation is to develop a three-dimensional (3-D) MC model in which the whole region of the HAZ around the weld pool is considered. By incorporating the calculated thermal history data at each site into the three-dimensional MC model, the simulated grain growth kinetics at each site will thus be strictly based on the corresponding thermal history — Fig. 1. Therefore, the detailed thermal and grain topological environment at each site in the actual weldment can be taken into account. Furthermore, a simulated 3-D real-time map of grain structure distribution around the weld pool can be established by relating the grain growth extents at various locations with their temperature-time histories, as well as grain topological environments. This simulated 3-D real-time grain distribution map can provide detailed insight in understanding the grain growth phenomena under the steep temperature gradient and transient thermal cycles that could not be obtained otherwise.

The work reported here is the first attempt to systematically model the complex welding phenomena involving heat transfer and fluid flow, phase transition and grain growth. The ability to predict both the geometry of the weld pool and important microstructural features indicates significant promise for understanding both macro and microstructures of titanium welds from the combination of the fundamental principles from both transport phenomena and phase transformation theory.

## Experimental Procedures

### Welding

Grade 2 commercially pure titanium bar of 10.2 cm diameter was welded by gas tungsten arc (GTA) welding. The composition of the as-received bar was (in wt-%): 0.14% Fe, 0.17% O, 0.03% Al, 0.02% Cr, 0.08% C, 0.001% H, 0.014% N, 0.02% Ni, 0.005% V and 0.004% Si. Gas tungsten arc welds were made at a constant power of 1.9 kW (100 A, 19 V), and extra high-purity helium (99.999%) was used as both the welding and shielding gas. The titanium bar was rotated at a constant speed of 0.20 rpm below the fixed electrode, which corresponds to a surface welding speed of 1.1 mm/s. Additional details about the welding procedure are reported in Refs. 20–23.

### Spatially Resolved X-Ray Diffraction

A schematic diagram of the SRXRD experimental setup is shown in Fig. 2. The SRXRD experiments were performed on the 31-pole wiggler beam line (Ref. 31), at Stanford Synchrotron Radiation Laboratory (SSRL) with Stanford Positron-Electron Accumulation Ring (SPEAR) operating at an electron energy of 3.0 GeV and an injection current of ~100 mA. The focused monochromatic synchrotron beam (8.5 keV) was passed through a 180-μm tungsten pinhole to render a 200-μm beam on the sample at an incident angle of ~25 deg. Additional details about the synchrotron beam are available in the literature (Refs. 20–23). The welding assembly was integrally mounted to a translation stage driven by a stepper motor with 10-μm precision and placed inside the environmental chamber to prevent oxidation of the titanium during welding. Spatial mapping of the phases in the HAZ was performed using the translation stage to manipulate the weld (welding torch and workpiece) with respect to the fixed X-ray beam in order to probe discrete regions around the weld. Movements perpendicular to

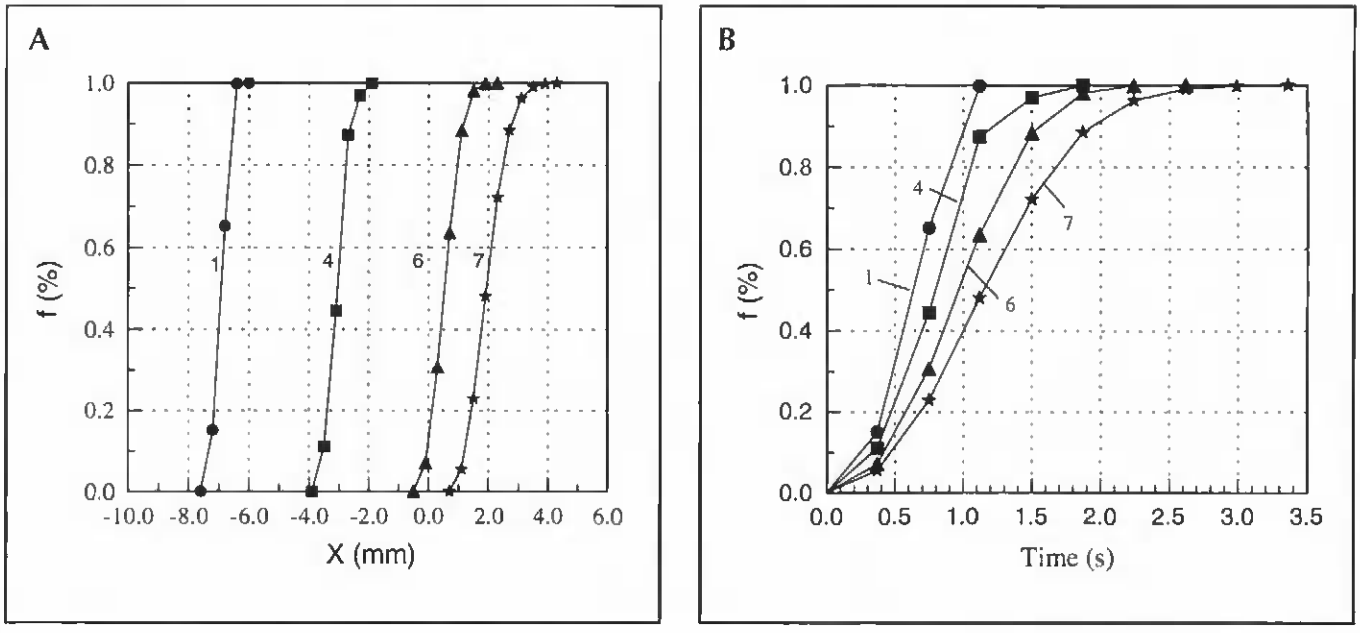


*Fig. 9 — A — Calculated β phase transformation along temperature-time profiles given in Fig. 7; B — calculated times needed for α→β transformation at different lines.*

the centerline of the weld were controlled by a computer and were achieved by direct translation of the workpiece with respect to the X-ray probe. A typical SRXRD run consisted of gathering 40 diffraction patterns at 200 μm apart along a predetermined path to span a range of 8 mm through the HAZ.

SRXRD data were taken during welding by positioning the beam at a fixed location with respect to the welding electrode and collecting data for 6 s per diffraction scan while the bar rotated under the torch at a constant speed. Up to 40 scans were taken during one revolution of the weld around the cylinder by incrementally jogging the weld in 200-μm steps to new locations at 6-s intervals. In this way a series of X-ray diffraction patterns was collected for a given weld along a direction perpendicular to and away from its centerline, and thus spanning an 8-mm range through the HAZ. Results of the sequential linear X-ray diffraction measurements made perpendicular to the welding direction were combined to construct a phase transformation map around the liquid weld pool.

#### Material Characterization

Optical metallography was performed on postweld samples using conventional polishing and etching techniques. Etching was performed in a chemical bath of 15 parts lactic acid, 5 parts nitric acid and 1 part hydrofluoric acid. To quantitatively describe the grain size gradient in the HAZ, the mean grain sizes at various distances from the weld interface were measured using lineal intercept method (Ref. 32) by placing test lines parallel to the weld interface. Because of significant grain size gradient in the HAZ, different magnifications in the range of 20X to 100X were used depending on the locations from the weld interface to ensure accurate grain size measurements.

## Mathematical Modeling

#### Calculation of Heat Transfer and Fluid Flow

Governing Equations

The heat transfer and fluid flow were calculated by numerical solution of the equations of conservation of mass, momentum and energy in three-dimensional form. In this work, the transient problem was transformed into a steady-state problem by solving in a coordinate system, which moves with the heat source (Ref. 5). In the moving coordinate system, the velocity and enthalpy fields are independent of time. As a consequence, the time required for computation is reduced significantly. The velocity transformation used and the transformed continuity, momentum and energy equations can be expressed as follows:

$$V' = V + V_s \tag{1}$$

$$\nabla \cdot V = 0 \tag{2}$$

$$\rho \nabla \cdot (VV) = -\nabla P + \mu_{eff} \nabla \cdot (\nabla V) + (S_v - \rho \nabla \cdot (V_s V)) \tag{3}$$

$$\rho \nabla \cdot (Vh) = \nabla \cdot \left( \frac{K_{eff}}{C_p} \nabla h \right) + S_l + S_h - \rho \nabla \cdot (V_s h) \tag{4}$$

where $V'$, $V$ and $V_s$ are the net velocity at any point, the convective component of the liquid metal velocity and the welding velocity, respectively $\rho$ is the density; $P$ is the effective pressure; $C_p$ is the specific heat; $S_V$ is the source term that takes into account the combined effect of buoyancy force, Marangoni stress and electromagnetic force; $h$ is the enthalpy; $S_h$ is the source term that takes into account the heat input from the welding source and the convective and radiative heat loss; $S_l$ is the source term that accounts for latent heat of melting and convective transport of latent heat; $\mu_{eff}$ is the effective viscosity; and $k_{eff}$ is the effective thermal conductivity.

An important component in the present heat transfer and fluid flow model is the incorporation of K - ε model to calculate the turbulent fluid flow and heat transfer in the weld pool under the present welding conditions. A detailed description of the K - ε model is given by Launder and Spalding (Ref. 33). Only the salient features of the model are presented here. The effects of turbulence on the fluid flow and heat transfer were included through the use of effective viscosity and thermal conductivity. The effective viscosity and thermal conductivity can be expressed as

$$\mu_{eff} = \mu_l + \mu \tag{5}$$

$$k_{eff} = k_l + k \tag{6}$$

**Table 1 — Data Used for the Calculation of Velocity and Temperature Fields**

| Physical Property | Value |
|---|---|
| Liquidus temperature (K) | 1941.0 |
| Solidus temperature (K) | 1941.0 |
| Density of liquid metal (kg/m$^3$) | 4400.0 |
| Viscosity of liquid (kg/m.s.) | $6.0 \times 10^{-3}$[a] |
| Thermal conductivity of solid (J/m-s-K) | 28.0 |
| Thermal conductivity of liquid (J/m-s-K) | 28.0[a] |
| Specific heat of solid (J/kg-K) | 700.0 |
| Specific heat of liquid (J/kg-K) | 700.0[a] |
| Latent heat of melting (J/kg) | $292.6 \times 10^3$ |
| Temperature coefficient of surface tension (N/m-K) | $-0.26 \times 10^{-3}$ |

[a] Estimated due to no values available for these data in the literature.

where $\mu_t$ and $k_t$ are the turbulent values, and $\mu$ and k are the molecular values. Unlike the molecular viscosity and thermal conductivity, which are physical properties, the turbulent viscosity and thermal conductivity are the properties of both the fluid and the flow system. The turbulent viscosity was calculated by

$$\mu_t = \frac{C_\eta \rho K^2}{\varepsilon} \tag{7}$$

where $C_\eta$ is an empirical constant, K is the turbulent kinetic energy and $\varepsilon$ is the dissipation rate of turbulent kinetic energy. The value of turbulent viscosity can be determined through solution of the equations of conservation of K and $\varepsilon$ as following:

$$\rho\frac{DK}{Dt} = \frac{1}{\sigma_k}\left\{\frac{\partial}{\partial x}\left[\mu_t\frac{\partial K}{\partial x}\right]+\frac{\partial}{\partial y}\left[\mu_t\frac{\partial K}{\partial y}\right]+\frac{\partial}{\partial z}\left[\mu_t\frac{\partial K}{\partial z}\right]\right\}+\mu_t G_k-\varepsilon \tag{8}$$

$$\rho\frac{D\varepsilon}{Dt} = \frac{1}{\sigma_\varepsilon}\left\{\frac{\partial}{\partial x}\left[\mu_t\frac{\partial \varepsilon}{\partial x}\right]+\frac{\partial}{\partial y}\left[\mu_t\frac{\partial \varepsilon}{\partial y}\right]+\frac{\partial}{\partial z}\left[\mu_t\frac{\partial \varepsilon}{\partial z}\right]\right\}+\frac{\varepsilon}{K}\left(C_1G_k-C_2\rho\varepsilon\right) \tag{9}$$

where $\sigma_k$, $\sigma_\varepsilon$, $C_1$ and $C_2$ are empirical constants and $\mu_t G_k$ is the turbulent counterpart to the viscous dissipation (Ref. 33). The turbulent thermal conductivity is related to the turbulent viscosity by the turbulent Prandtl number (Refs. 18, 33). $Pr_t = C_p\mu_t/k_t = 0.9$. Thus, the spatial distribution of viscosity and thermal conductivity of the liquid metal could be calculated from the turbulence model.

## Boundary Conditions

The calculations were carried out in a Cartesian coordinate system, and only half of the workpiece was considered since the weld pool is symmetrical. Lin and Eagar (Ref. 51) calculated the maximum depth of weld pool surface depression to be 1.3 mm at 300 A during GTA welding. They pointed out that at low currents the surface of GTA weld pools is essentially flat. Since the experiments reported in this paper were conducted at 100 A, the surface of the weld pool was essentially flat. Along the vertical plane of symmetry (y = 0 plane), the boundary conditions for the velocity components were defined as

$$\frac{dV_x}{dy} = 0 \tag{10.1}$$

$$V_y = 0 \tag{10.2}$$

$$\frac{dV_z}{dy} = 0 \tag{10.3}$$

where $V_x$, $V_y$ and $V_z$ are the components of the convective velocity V in the x, y and z directions. The z component of the velocity, $V_z$, was defined to be zero at the top surface. The x and y components of the velocity vector on the top surface (z = 0 plane) were determined by the Marangoni stress and were defined as

$$-\mu_{eff}\frac{dV_x}{dz} = f_l\frac{d\gamma}{dT}\frac{dT}{dx} \tag{11.1}$$

$$-\mu_{eff}\frac{dV_y}{dz} = f_l\frac{d\gamma}{dT}\frac{dT}{dy} \tag{11.2}$$

where $d\gamma/dT$ is the temperature coefficient of surface tension and $f_l$ is the liquid fraction, which is assumed to vary linearly with temperature in the mushy zone. The velocity in the solid region was set to be zero.

On the top surface (z = 0 plane), the heat exchange between the heat source and the surface of the sample and the radiative and convective heat loss to the surrounding were prescribed as

$$J_h(\xi,y,z)_{z=0} = \frac{q\eta}{2\pi r_b^2}e^{\left[\frac{(\xi^2+y^2)}{2r_b^2}\right]} - \varepsilon_1\sigma\left(T(\xi,y,z)_{z=0}^4 - T_g^4\right) - h_c\left(T(\xi,y,z)_{z=0} - T_g\right) \tag{12}$$

where q is the power input, $\eta$ is the welding process efficiency, $r_b$ is the arc radius, $T(\xi,y,z)_{z=0}$ is the local weld pool surface temperature, $T_g$ is ambient temperature, $\varepsilon_1$ is the emissivity, $\sigma$ is the Stefan-Boltzmann constant and $h_c$ is the heat transfer coefficient. At the plane of symmetry (y = 0 plane), the gradient of the enthalpy was defined as

$$\frac{dh}{dy} = 0 \tag{13}$$

At other surfaces of the system, the enthalpy was prescribed by setting the temperature as the ambient temperature.

The boundary conditions for K and $\varepsilon$ at the vertical symmetry plane (y = 0 plane) were defined as $\partial K/\partial y = 0$ and $\partial\varepsilon/\partial y = 0$, and at the top surface (z = 0 plane): $\partial K/\partial z = 0$ and $\partial\varepsilon/\partial z = 0$. At the solid-liquid interface, the values of K and $\varepsilon$ were taken to be zero.

## Solution Procedure

The governing equations were represented by a set of finite difference equations and solved iteratively on a line by line basis utilizing a tri-diagonal matrix algorithm. The details of the procedure are described elsewhere (Ref. 34). The dimensions of the solution domain were 32.0 (length) x 6.3 (width) x 5.1 (thickness) cm$^3$. A 56 x 30 x 25 grid system was used in the calculations. Spatially nonuniform grids were used for maximum resolution of variables. Finer grid spacing was used near the heat source. The minimum grid spacing was 0.005 cm directly below the weld pool surface. The data used for the calculation of the fluid flow and heat transfer are presented in Table 1.

## Calculation of Thermal Cycle

After the solution of the transformed momentum and energy equations, a steady-state temperature field can be obtained. At any given locations (x, y, z), the temperature variation with time can be expressed as

$$T(x,y,z,t_2) = \frac{Ts(\xi_2,y,z)-Ts(\xi_1,y,z)}{\xi_2-\xi_1}V_s(t_2-t_1) + T(x,y,z,t_1) \tag{14}$$

where $Ts(\xi_2, y, z)$ and $Ts(\xi_1, y, z)$ are the steady-state temperatures at coordinates $(\xi_2, y, z)$ and $(\xi_1, y, z)$, respectively, $\xi_2 - \xi_1$ is the distance traveled by the arc in time $(t_2-t_1)$, $V_s$ is the welding speed and $T(x,y,z,t_2)$ and $T(x,y,z,t_1)$ are the temperatures at times $t_1$ and $t_2$, respectively.

### Phase Transformation Calculation

## Possible Mechanisms

The $\alpha$-$\beta$ phase transformation in titanium can occur by martensitic (Ref. 35), massive (Refs. 35–38) or classical nucleation and growth (Refs. 35, 38) mecha-

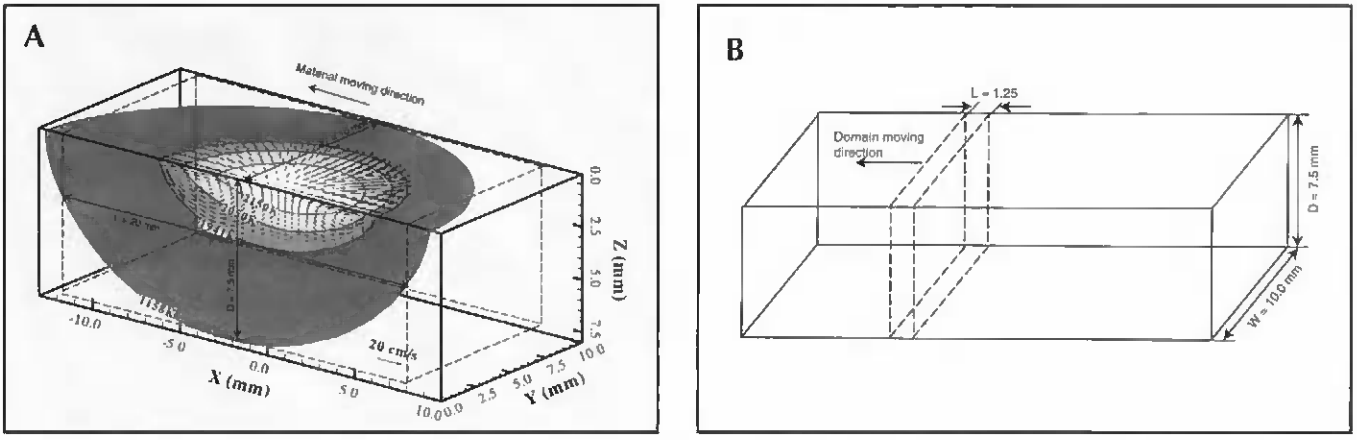


*Fig. 10 — A — Domain selected for simulation of grain structure evolution in the HAZ. The length (L), width (W) and depth (D) of the selected domain are 20, 10 and 8 mm, respectively. The corresponding grid system used for the MC model is 400 x 200 x 160. B — Domain selected for simulation of grain structure evolution in the HAZ. The selected domain is assumed to move from the location where grain growth begins to the location where grain growth ends. The length (L), width (W) and depth (D) of the selected domain are 1.25, 10 and 7.5 mm, respectively. The corresponding grid system used for the MC model is 50 x 400 x 300.*

nisms. These mechanisms compete with one another, and the mechanism that is ultimately responsible for the phase transformation depends on the purity of the titanium, its microstructure and the thermal processing conditions. The martensitic phase transformation occurs only at high rates and has been reported to take place at cooling rates in excess of 3000 K/s (Ref. 35). This cooling rate far exceeds those encountered in conventional arc welds and precludes this mechanism. Massive transformations in titanium have been reported to occur at cooling rates similar to those of martensitic transformations (Ref. 35), but also at cooling rates well within the realm of arc welds (Ref. 38). Conventional nucleation and growth phase transformations with long-range solute partitioning occur only at low cooling rates and are generally believed to occur with much slower kinetics than massive transformations (Refs. 36, 37).

In a previous investigation, SRXRD was used as an *in-situ* experimental technique to map the phases that exist around an arc weld in commercially pure titanium (Ref. 20). This phase map contains direct evidence of the α→β transformation kinetics in the form of spatial displacements of the product phase with respect to the thermodynamic transformation isotherm. Results of this study showed the α→β transformation during heating took place with slower kinetics than the β→α transformation during cooling. From the SRXRD measurements, the β→α transformation was estimated to occur with an interface velocity of 100 μm/s (Ref. 20), which is consistent with measured interface velocities of massive transformation in dilute titanium alloys (Ref. 36). Since massive β→α transformations during cooling of titanium and titanium alloys have been well documented by other investigators (Refs. 35–38), this mechanism was assumed to be responsible for the β→α transformation during cooling in titanium arc welds. The α→β transformation, on the other hand, was estimated by the SRXRD measurements to occur at rates more consistent with long-range diffusional growth (Ref. 20), but a thorough investigation of this mechanism was not performed. Since the α→β transformation has not been documented nearly as well as the β→α transformation in the available literature, the transformation kinetics need to be studied in more detail. Here, we utilize isotherms calculated from the turbulent fluid flow and heat transfer model as input to a modified JMA kinetic model to study the possible rate-controlling steps for the α→β phase transformation.

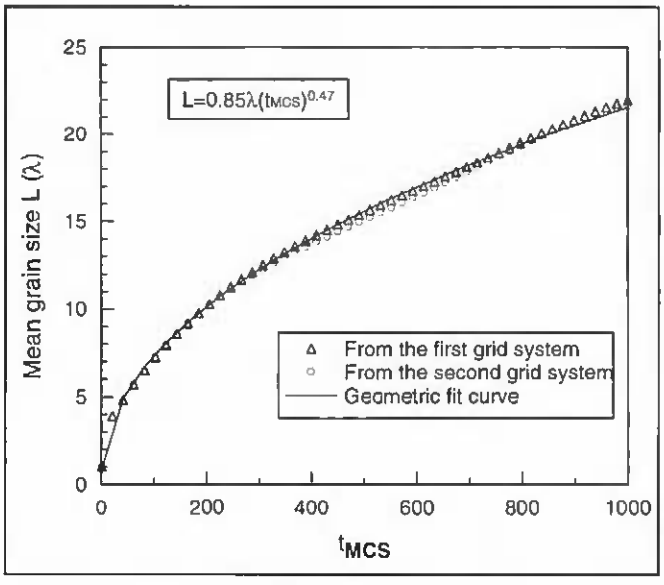


*Fig. 11 — Simulated grain growth kinetics from the MC model. Both of the mean grain size L and Monte Carlo simulation time $t_{MCS}$ are dimensionless quantities in this figure.*

The principal impurities in the Grade 2 titanium are O (0.17 wt-%) and Fe (0.14 wt-%). In the previous study, the presence of Fe-rich bcc/omega phase particles distributed throughout the grains was observed in the starting titanium microstructure (Ref. 20). These pre-existing particles appear to provide growth sites for the α→β transformation and also tie up much of the Fe impurities. Therefore, it is likely the α→β transformation during arc welding takes place by a growth dominated mechanism whereby nucleation of the β phase is not necessary. Since the α→β transformation could be controlled either by diffusion of titanium or oxygen atoms across the α/β interface, or oxygen atoms long-range diffusion, each of these possible scenarios will be modeled to determine which

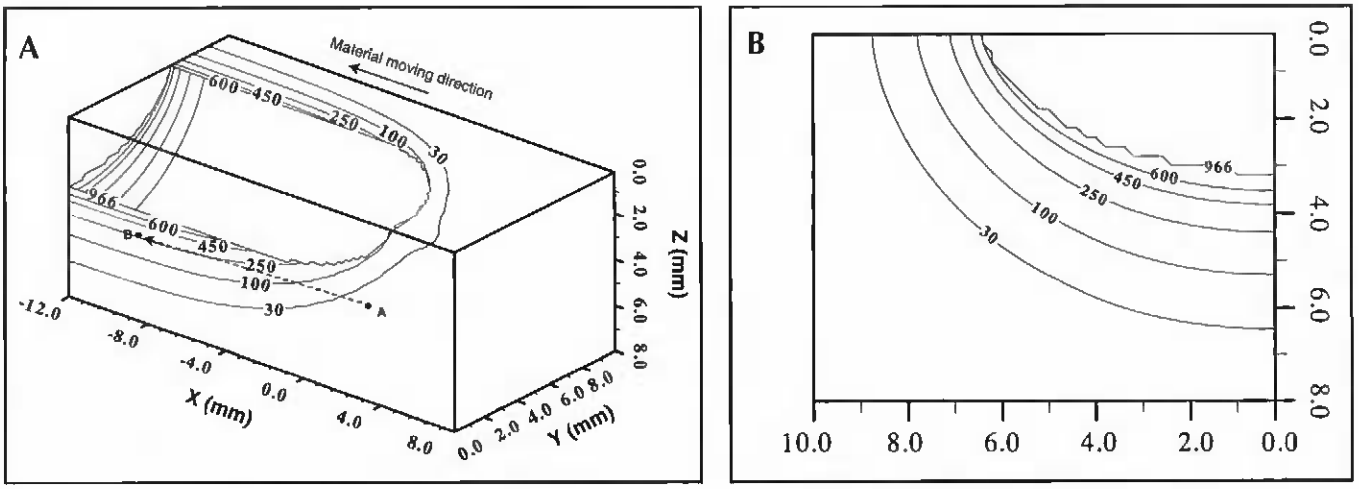


*Fig. 12 — A — Monte Carlo simulation time $t_{MCS}$ spatial distribution in the domain ( 20 x 10 x 8 mm³); B — Monte Carlo simulation time $t_{MCS}$ spatial distribution in the cross section of the domain (x = –12 mm).*

**Table 2 — Kinetic Data Used for the Calculation of the α ⇻ β Phase Transformation for Different Proposed Mechanisms**

| Scenarios | Assumed mechanisms | n | $K_0$ | ΔG (k)/*mol* |
|---|---|---|---|---|
| I | Titanium short-range diffusion (interface controlled) | 3.0 | $2.18 \times 10^6$ | 152.7 (Ref. 44) |
| II | Oxygen short-range diffusion (interface controlled) | 3.0 | $2.18 \times 10^6$ | 138.2 (Ref.49) |
| III | Oxygen long-range diffusion | 1.5 | $2.18 \times 10^6$ | 138.2 (Ref. 49) |

is the most likely to control the α→β transformation rate. The three different scenarios can be summarized as 1) an interface controlled mechanism with titanium short-range diffusion (across the α/β interface), 2) an interface-controlled mechanism with oxygen short-range diffusion (across the α/β interface) and 3) a long-range solute partitioning mechanism with oxygen diffusion.

Application of JMA Equation

The JMA equation is suitable for describing the kinetics of reactions controlled by the nucleation and growth mechanism (Refs. 39, 40). Therefore, this equation is applicable to describe the α→β transition in titanium for all the mechanisms assumed in the above three scenarios. The JMA equation under isothermal conditions can be expressed as (Ref. 24)

$$f=1-\exp\{-[k(T)(t-t_0)]^n\} \qquad (15)$$

where n is a numerical exponent whose value is determined by the nucleation mode and the dimensions of the growing particles (Ref. 41). It is a constant independent of temperature, provided there is no change in the nucleation mechanism. On the other hand, k(T) depends on both the nucleation and growth rates and is therefore highly sensitive to temperature

$$k(T)=k_0\times\exp\left(-\frac{\Delta G(T)}{k_B T}\right) \qquad (16)$$

where ΔG(T) is the total activation energy for nucleation and growth, $k_0$ is pre-exponential constant and $k_B$ is the Boltzmann constant. Since heterogeneous nucleation is assumed in the JMA equation, the values of k(T), ΔG(T) and $k_0$ are usually determined by isothermal experiments.

The JMA equation can be modified for the nonisothermal kinetics (Ref. 24). The proposed method used the discretization of the time dependence of the temperature, *i.e.*, approximation of the continuous temperature-time curves by many isothermal steps, each of them obeying the isothermal JMA-kinetics. The detailed procedure to derive the modified JMA equation is available in the literature (Ref. 24). The final expression for the transformed fraction obtained from m subsequent isothermal steps can be expressed as

$$f(t(T))=1-\exp\left\{-\left[\sum_{i=0}^{m-1}k(t_0+i\Delta T)\Delta t\right]^n\right\} \qquad (17)$$

where f(t(T)) stands for the transformed phase fraction under nonisothermal conditions, Δt is the time step, ΔT is the temperature change corresponding to each Δt, $T_0$ is the initial temperature, k is a temperature-dependent constant and m is the total number of the subsequent isothermal steps.

In order to use Equation 17, the temperature dependence of the transformation rate k(T) and the exponent n have to be specified. The values of k(T) and n are dependent on the transition mechanism assumed. If the transport of Ti atoms across the interface is considered to be the limiting step, then the activation energy of the titanium self-diffusion could be taken as the value of ΔG(T) in Equation 16 to calculate k(T). If the transport of oxygen atoms across the interface is considered to be the limiting step, then the activation energy of the oxygen diffusion in titanium could be taken as the value of ΔG(T). In both cases, it is assumed that the pre-existing Fe-stabilized bcc/omega phase particles (Ref. 20) provide a sufficient density of growth sites so that nucleation of β particles from the α matrix is not required. Under these zero-nucleation-rate conditions, a value of n = 1.5 can be assumed for the JMA nucleation mode exponent for long-range diffusion and n = 3.0 can be assumed for interface-controlled growth (Ref. 41).

The kinetic data used in the JMA model is summarized in Table 2 for three different scenarios. In all three mechanisms, the pre-exponential constant $k_0$ in Equation 16 took the same value. This value was estimated from the experimental data in the literature (Ref. 35) and was found to be 2.1B x $10^6$. For the purpose of this paper, $k_0$ will be taken to be

a constant for the α→β transformation since the temperature dependence of $k_0$ is not known for titanium and also it is believed the temperature dependence of $k_0$ can be considered to be small compared to the exponential term in Equation 16 (Ref. 42).

### Grain Growth Prediction by Monte Carlo Simulation

The methodologies of using the MC technique to simulate grain growth have been given in detail in the literature (Refs. 25–29). Only the salient features to apply this technique to simulate grain growth in the HAZ are described here. To apply the MC technique to a real metallurgical phenomena, the conversion of the MC simulation time ($t_{MCS}$) to real time is necessary. Depending on the nature of the problem, different methods (Ref. 28) have been used to convert $t_{MCS}$ to real time. When the isothermal grain growth data for the given material are insufficient, such as grain growth in pure titanium, the grain boundary migration model (GBM) proposed by Gao, *et al.* (Ref. 28), can be used to establish the relation between $t_{MCS}$ and real time-temperature kinetics. In the GBM model, the grain growth exponent is taken as 0.5. The isothermal grain growth kinetics in beta-titanium are available in the literature and the grain growth exponent was found (Ref. 52) to be approximately 0.5. This value justifies the application of grain boundary migration model to simulate grain growth in commercially pure titanium.

#### Relation between $t_{MCS}$ and Real-Time-Temperature

Through the MC simulation, an empirical relation between the simulated grain size and the MC simulation time can be obtained as (Ref. 28)

$$L = K_1 \times \lambda \times (t_{MCS})^{n_1} \qquad (18)$$

where L is the dimensionless simulated grain size measured by mean grain intercepts, λ is the discrete grid point spacing in the MC technique, $t_{MCS}$ is MC simulation time or MC simulation iteration steps, and $K_1$ and $n_1$ are the model constants, which are obtained by regression analysis of the data generated from MC simulation. It should be noted Equation 18 represents the intrinsic grain growth kinetics of the MC model. The grain growth kinetics so obtained are dependent only on the grid system of the MC model and independent of material properties and temperature-time history. The simulated mean grain size (L) and the MC simulation time ($t_{MCS}$) in Equation 18 are dimensionless quantities. To simulate grain growth of a specific material under specified thermal conditions, a relation needs to be established between $t_{MCS}$ and the given conditions, such as the material properties and temperature-time history.

Based on the well known parabolic law for isothermal grain growth (Ref. 30) and the assumptions of grain boundary migration made by Porter, *et al.* (Ref. 43),and Gao, *et al.* (Ref. 28), an analytical equation was derived from the first principles to describe the isothermal grain growth kinetics

$$L^2 - L_0^2 = \left\{\frac{4\gamma_b A Z V_m^2}{N_a^2 h_p} \times \exp\left(\frac{\Delta S_a}{R}\right)\right\} \times \exp\left(\frac{-Q}{RT}\right) \times t \qquad (19)$$

where L is the average grain size at time t, $L_0$ is the initial average grain size, $\gamma_b$ is the grain boundary energy, A is the accommodation probability, Z is the average number of atoms per unit area at grain boundary, $V_m$ is the atomic molar volume, $N_a$ is Avagadro's number, $h_p$ is Planck's constant, $\Delta S_a$ is the activation entropy, Q is the activation energy for grain growth, T is the absolute temperature, R is the gas constant and t is time. In the present investigation, the value of initial grain size (Ref. 20) $L_0$ is about 25 μm. The data of activation energy Q for grain growth in titanium is not available in the literature. However, the value of activation energy for grain growth usually ranges from ½ to ⅔ of that for bulk diffusion (Ref. 43). Here we take approximately ⅔ of the activation energy of Ti atom bulk diffusion (Ref. 44) (153.0 kJ/mol) as the value of that for grain growth. The grain boundary energy has been assumed to be a constant and independent of temperature (Refs. 25–29). The data of titanium grain boundary energy is not available in the literature, but was estimated to be 0.75 J/m², as indicated by the procedure given in the appendix. The value of $V_m$ can be calculated based on the density and atomic weight of titanium. The activation entropy for grain boundary migration, $\Delta S_a$, can be assumed (Ref. 28) to be equal to the fusion entropy of the material, $\Delta S_f$. The value of $\Delta S_f$ for titanium (Ref. 46) is 7.21 J·mol$^{-1}$·K$^{-1}$. The data used for the modeling grain growth are listed in Table 3.

Equation 19 can be further extended for grain growth under nonisothermal conditions by differentiating and then integrating it over the continuous thermal cycles. If we assume that γ and $\Delta S_a$ are independent of temperature, $K_2$ in Equation 20, which equals all terms within

**Table 3 — Data Used for the Calculation of the β Grain Growth Kinetics**

| | |
|---|---|
| Initial average grain size, $L_0$ | 25 μm |
| Activation energy for grain growth, Q | $1.02 \times 10^5$ J/mol |
| Grain boundary energy, $\gamma_b$ | 0.75 J/m² |
| Accommodation probability, A | 1.0 |
| Average number per unit area at grain boundary, Z | $2.0 \times 10^{19}$ atoms/m² |
| Atomic molar volume, $V_m$ | $1.1 \times 10^{-5}$ m³/mol |
| Activation entropy, $\Delta S_a$ | 7.21 J/mol-K |
| Avagadro's number, $N_a$ | $6.02 \times 10^{23}$ mol$^{-1}$ |
| Planck's constant, $h_p$ | $6.624 \times 10^{-34}$ J · s |

**Table 4 — Calculated Peak Temperatures and Overall Times over the α/β Isotherm at the Seven Different Locations**

| Location No. | 1 | 2 | 3 | 4 | 5 | 6 | 7 |
|---|---|---|---|---|---|---|---|
| Distance[a] (mm) | 4.2 | 5.8 | 6.6 | 8.2 | 8.8 | 9.2 | 9.6 |
| $T_{peak}$ (K) | 2186 | 2019 | 1835 | 1483 | 1347 | 1287 | 1233 |
| $t_{total}$ (s)[a] | 20.0 | 18.1 | 16.6 | 13.1 | 10.6 | 9.0 | 7.1 |

(a) Distance here indicates the distance from the location to the weld centerline; $t_{total}$ here represents the total time above the α/β isotherms.

**Table 5 — Comparison of the Calculated and Experimental Times Necessary for the Completion of α ⇆ β Transformation at Different Locations**

| Location | | 1 | 2 | 3 | 4 | 5 | 6 | 7 |
|---|---|---|---|---|---|---|---|---|
| Times from phase distribution map (s) | | 1.25 | 1.45 | 1.60 | 1.91 | 2.26 | 3.05 | 3.91 |
| Calculated times under different conditions (s) | Mechanism-1 | 1.20 | 1.35 | 1.51 | 1.75 | 2.14 | 2.62 | 3.36 |
| | Mechanism-2 | 0.85 | 0.93 | 1.02 | 1.12 | 1.28 | 1.50 | 1.65 |
| | Mechanism-3 | 1.12 | 1.30 | 1.45 | 1.65 | 1.95 | 2.24 | 2.62 |

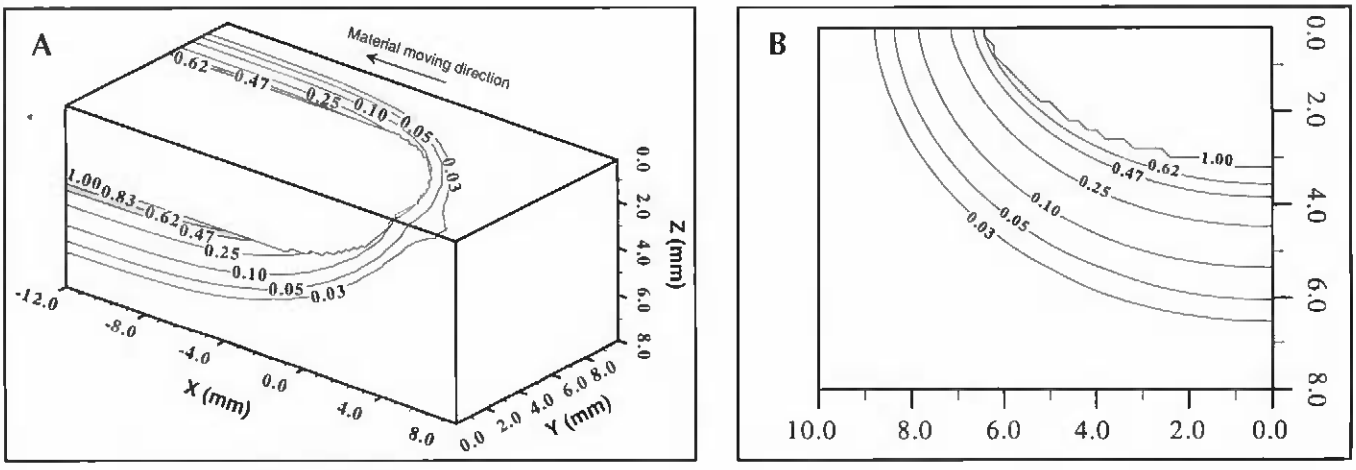


*Fig. 13 — A — Site selection probability spatial distribution in the domain (20 x 10 x 8 mm³); B — site selection probability spatial distribution in the cross section of the domain (x = –12 mm).*

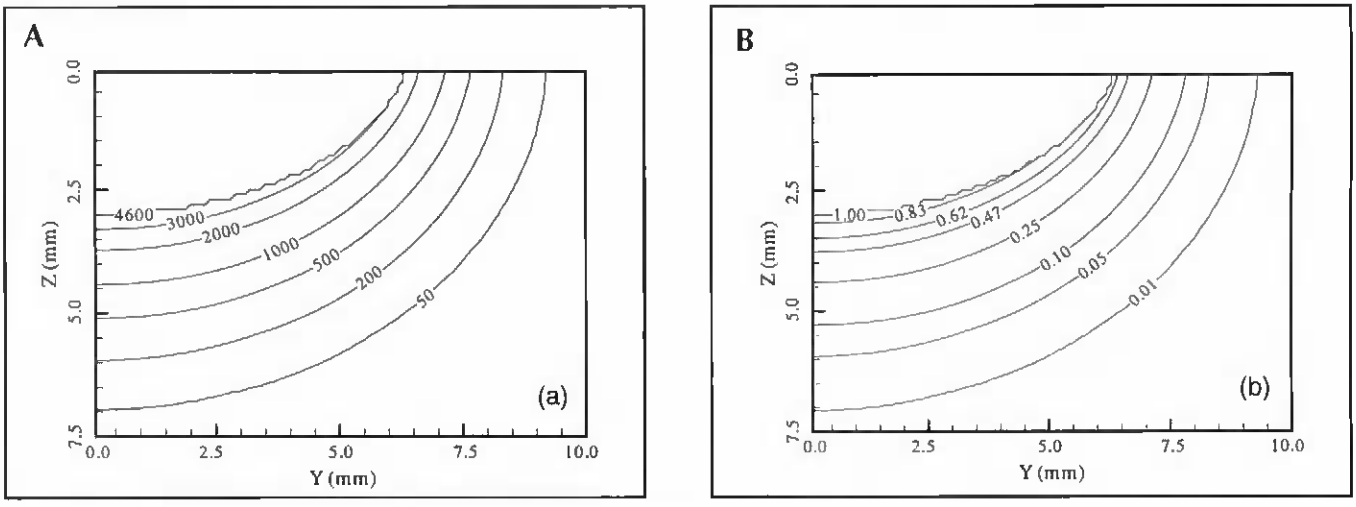


*Fig. 14 — Monte Carlo simulation time $t_{MCS}$; B — site selection probability spatial distribution at the cross section of the second domain (1.25 x 10 x 7.5 mm³).*

bracket in Equation 19 as a constant and the grain growth kinetics during continuous heating and cooling, can be expressed as

$$L^2 = L_0^2 + K_2 \sum_{i=1}^{m} \left[ \Delta t_i \times \exp\left( -\frac{Q}{RT_i} \right) \right] \quad (20)$$

where $\Delta t_i$ and $T_i$ are the time step and the corresponding temperature, respectively. Equating the mean grain size from Equation 20 to that from Equation 18, the MC simulation time can be related with the real time and temperature and expressed as

$$(t_{MCS})^{2n_1} = \left( \frac{L_0}{K_1 \lambda} \right)^2 + \frac{K_2}{(K_1 \lambda)^2} \sum_{i=1}^{m} \left[ \Delta t_i \times \exp\left( -\frac{Q}{RT_i} \right) \right] \quad (21)$$

Thus, the $t_{MCS}$ necessary to achieve a specific mean grain size during a non-isothermal process can be determined by incorporating the corresponding thermal cycle into Equation 21. Since the thermal cycle in the HAZ varies depending on its location, the corresponding $t_{MCS}$ varies at each site. The higher the temperature or the longer the time period for grain growth at a site, the higher the value of $t_{MCS}$ expected at that site.

Site Selection Probability

The $t_{MCS}$ variation at different locations, calculated from Equation 21, cannot be directly applied in the MC algorithm because the $t_{MCS}$ is a measure of time in the MC algorithm. To solve this problem, a concept of site selection probability is introduced. The site selection probability varies depending on the time-temperature history at any given location. The larger the $t_{MCS}$ at a site, the higher the corresponding site selection probability, p(r)

$$p(r) = \frac{t_{MCS}}{t_{MCS}^{max}} \quad (22)$$

where $t_{MCS}$ is the MC simulation time at any site in the region and $t_{MCS}^{max}$ is the maximum value of the MC simulation time in the computational domain. Both $t_{MCS}$ and $t_{MCS}^{max}$ can be calculated from Equation 21 from the calculated thermal cycles at the corresponding locations. The $t_{MCS}$ variation can thus be transformed into the variation of site selection probability and applied in the MC model. Thus, the spatial variation of thermal cycles is included in the site selection probability.

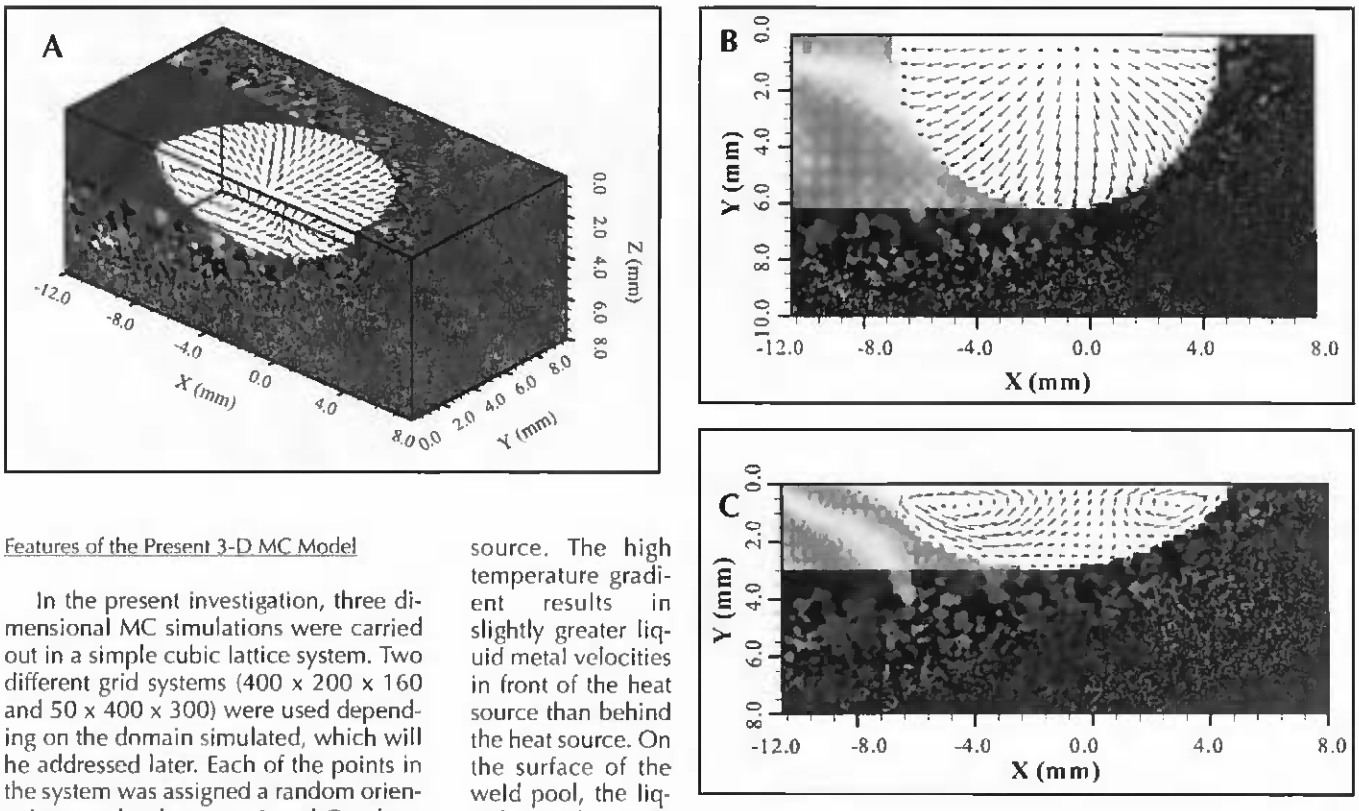


*Fig. 15 — A — Real-time mapping grain structure distribution around the weld pool in three dimensions using 400 x 200 x 160 grids (the grid spacing is 50 μm); B — top view of grain structure distribution around the weld pool; C — side view of grain structure distribution around the weld pool.*

Features of the Present 3-D MC Model

In the present investigation, three dimensional MC simulations were carried out in a simple cubic lattice system. Two different grid systems (400 x 200 x 160 and 50 x 400 x 300) were used depending on the domain simulated, which will he addressed later. Each of the points in the system was assigned a random orientation number between 1 and Q, where Q was the total number of grain orientations. The value of Q was taken to be 48 in the present simulation, since it is known (Ref. 24) the grain growth exponent becomes almost independent of Q when its value is larger than 30. The local energy was calculated by a shell of 26 grid points (Ref. 26) consisting of the first, second and third nearest neighhors. It should be pointed out that in the present MC model the new attempted orientation was limited to one of the nearest-neighbor orientations rather than all possible orientations in the system. This is because the grain boundary migration only results from the process that atoms close to the grain boundary jump into the nearest grain interior. The soundness of this method has been justified in the literature (Refs. 47–48).

## Results and Discussion

### Profiles and Geometry

The computed temperature and velocity fields in three dimensions considering turbulent transfer of heat and momentum are shown in Fig. 3. In this figure, the temperature field is indicated by contour lines and the velocity field is represented by the arrows. The general features of the calculated temperature field are consistent with the results reported in the literature (Ref. 2). In front of the heat source, the temperature gradient is greater than that behind the heat source. The high temperature gradient results in slightly greater liquid metal velocities in front of the heat source than behind the heat source. On the surface of the weld pool, the liquid metal moves from the center to the periphery. This is expected for a metal with a very low concentration of surface-active elements (*e.g.*, very low sulfur and low free-oxygen contents), which results in a negative temperature coefficient of surface tension $d\gamma/dT$ (Ref. 50). As the result of the outward fluid flow and heat transfer on the surface, the weld pool is wide and shallow.

The distributions of turbulent viscosity, thermal conductivity, kinetic energy and dissipation rate in the weld pool are shown in Fig. 4. These quantities are determined by the fluid motion in the weld pool. Since the welding current is not high under the present welding conditions, the electromagnetic force is weak and surface tension is the dominant force. Therefore, the circulation of the molten metal is most intense near the surface and the level of turbulence decreases progressively as the fluid approaches the solid surface. It is interesting that the maximum values of these variables do not lie in the middle of the weld pool. This is because the distributions of these variables are determined by the flow system, and the maximum velocity gradient does not occur in the middle in the present flow system. The maximum dimensionless viscosity ($\mu_t/\mu$) and thermal conductivity ($k_t/k$) values were found to be 13.5 and 4.0, respectively. The calculated dimensionless viscosity ($\mu_t/\mu$) and thermal conductivity ($k_t/k$) values and their spatial distribution patterns are comparable with those reported in the literature (Refs. 18, 19). The high values of these ratios indicate the dissipations of heat and momentum in the weld pool are significantly aided by turbulence. In some previous research on the simulation of heat transfer and fluid flow in the weld pool, the viscosity and thermal conductivity values were arbitrarily enhanced by a constant factor (Ref. 6). The rigorously computed turbulent viscosity and thermal conductivity values presented here clearly show these quantities vary strongly depending on the location within the weld pool. Therefore, accurate calculations of temperature and velocity fields must utilize an appropriate turbulence model.

The geometry of the fusion zone can be predicted from the calculated temperature field, shown in Fig. 5. The fusion zone was determined by the liquidus temperature (1941 K). The calculated width and depth of the fusion zone were found to be 12.2 mm and 2.9 mm, respectively. The corresponding experimental data were 12.0 ± 0.2 mm and 2.8 ± 0.2 mm, respectively. Thus, the calcu-

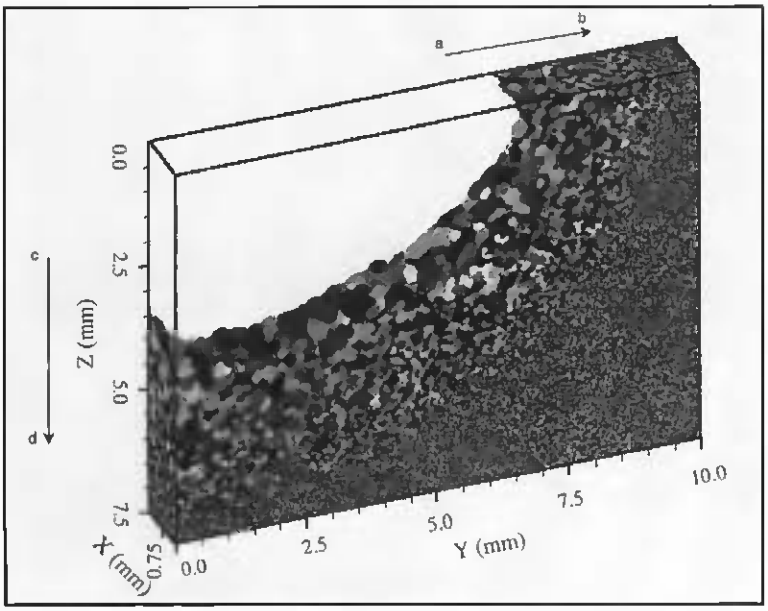


*Fig. 16 — Simulated final grain structure of the HAZ using 50 x 400 x 300 grids.*

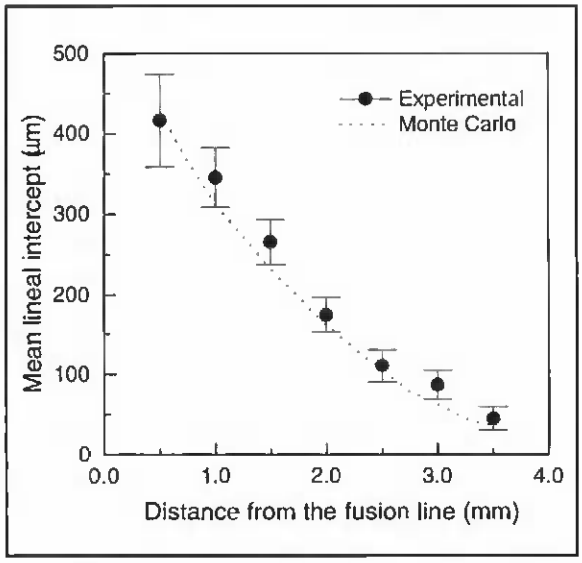


*Fig. 17 — Comparison of the calculated and experimental mean grain size at various locations along line ab on the surface of the weldment.*

lated dimensions of the FZ agreed well with the corresponding experimental results. Since the starting temperature for the annealing and recrystallization of α-Ti is not known, the geometry of the HAZ cannot be exactly predicted. However, the β-phase-containing region (α-Ti partially or fully transformed to β-Ti) in the HAZ can be predicted. This region exists between the α→β transition isotherm (1158 K) and the liquidus temperature (1941 K). The calculated width of this predicted β-phase-containing region on the top surface was about 3.8 mm, which equals to the corresponding experimentally measured width on the top surface as shown in Fig. 5. From Fig. 5, it can be observed that both the shape and size of this predicted β-phase-containing region are comparable with those of the experimental HAZ.

### Spatial Distribution of Phases

#### Experimental Phase Distribution Map

The spatial distribution map of phases (Ref. 20) as determined from the SRXRD data is shown in Fig. 6A, where the stationary welding electrode is positioned at X = Y = 0, with metal moving from left to right along the X-axis. Five different phase regions were identified in Fig. 6A: α-Ti, (α+β) mixed region, ($\alpha_B$+β) mixed region, β-Ti and liquid phase. The symbol $\alpha_B$ in the map denotes the back-transformed α-Ti from β-Ti during cooling. The experimental phase boundaries can be approximately determined, as shown by dashed lines in Fig. 6A. It should be noted that the phase distribution map in Fig. 6A is somewhat different from that in the previous paper (Ref. 20) in which the HAZ were subclassified into six regions. To focus on the issues investigated in the present paper, some subclassified regions in a previous investigation (*e.g.*, the annealed and recrystallized zone $\alpha_{AR}$, and the recrystallized zone undergoing grain growth $\alpha_{RG}$) are incorporated in the α-Ti region in Fig. 6A.

#### Calculated Phase Boundaries

The calculated isotherms of α/β (1158 K) and β/liquid (1941 K) phase transitions were imposed on the experimentally determined phase distribution map, as shown in Fig. 6B. It was found the calculated isotherms matched the phase distribution map very well. This means the phase boundaries of α/(α+β) and β/liquid can be satisfactorily predicted by the calculated temperature. The (α+β)/β phase boundary lies at the locations where α–Ti totally transformed to β-Ti, as indicated by the arrows in Fig. 6B. The prediction of the (α+β)/β phase boundary needs the knowledge of both thermal cycles and the kinetics of the transformation, and therefore cannot be predicted by the thermal model alone.

To predict the locations of the (α+β)/β phase boundary, a series of lines parallel to the welding direction were selected, as shown in Fig. 6B. These lines pass through the locations where the (α+β)/β phase boundary has been experimentally determined. As the material approaches the heat source, the α→β transition at different locations begins when the monitoring locations reach the α/β isotherm (1158 K). The extent of α→β phase transformation along these lines was calculated by the combination of the calculated thermal cycles and the modified JMA Equation 17. The calculated thermal cycles experienced by the material moving along these lines are shown in Fig. 7. From this figure, the peak temperatures and the time periods above the α/β isotherm along these lines can be obtained. The further the line is away from the welding centerline, the lower the temperature and the shorter the time period above the α/β transformation temperature. The peak temperatures and the time periods above the α/β isotherm along these lines are given in detail in Table 4.

After knowing the thermal cycles along the lines parallel to the welding direction, the extents of phase transformation along these lines can be calculated by Equation 17. Different transition mechanisms assumed were used to predict the (α+β)/β phase boundary by taking the corresponding values of n and ΔG(T) in Table 2. For each mechanism, the times for the completion of the α→β transformation along these lines were calculated. The calculated reaction times for all of the mechanisms are shown in Table 5. The time for the completion of the α→β transformation along a line parallel to the welding direction can also be obtained experimentally from the phase distribution map. In this way, the time was calculated by dividing the distance — between the α/β isotherm and the experimentally determined location of the (α+β)/β phase boundary along this line — by the welding speed.

To identify the possible mechanism for the α→β transformation, the calculated times for each assumed mechanism were compared with the times determined from the experimental phase distribution map, as shown in Fig. 8. It was found the times from the phase distribution map agreed well with the calculated times from mechanism 1, in which the α→β transition was assumed to be controlled by the transport of Ti atoms across the interface. The calculated times from mechanism 3, in which the transition was assumed to be controlled by oxygen long-range diffusion, are also approximately comparable with the experimentally determined times. Significant discrepancies exist between the experimental determined times and the calculated times from mechanism 2, in which the transition was assumed to be controlled by the transport of oxygen atoms across the interface. Through the comparison of the calculated times with the experimentally determined times, it seems that the α→β transition is most likely controlled by the transport of Ti atoms across the interface.

By adopting the mechanism that the α→β transformation was controlled by the transport of Ti atoms across the interface, the locations of the (α+β)/β phase boundary along the lines parallel to the welding direction were predicted. The transformed volume fractions of a phase along the lines were calculated by Equation 17 and shown in Fig. 9A. Depending on the thermal history experienced, the times for the completion of the α→β transformation along these lines were different. As expected, the further away the line from the welding centerline, the longer the time for the completion of the transformation. This can be more clearly observed by comparing the times needed for the α→β transformation along different lines, as shown in Fig. 9B. After obtaining the reaction times along these lines, the distances between the transformation starting points and the transformation finishing points can be calculated by multiplying the welding speed with the calculated reactions times. The starting points are the intercepts of the calculated α/β isotherm with these lines. Thus, the locations of the (α+β)/β phase boundary along these lines can be determined and shown as the plain circles in Fig. 6B.

### Grain Growth in the Single β Region

#### Domain Selection for MC Simulation

The selection of the domain for MC simulation of grain growth in the HAZ was based on the calculated temperature field from the 3-D heat transfer and fluid flow model. In order to achieve efficient simulation of grain growth, two factors need to be considered in selecting the simulation domain. First, all the essential geometric features of the HAZ should be included in the simulated domain. On the other hand, the domain should be kept as small as possible, because simulation of grain growth in the whole HAZ region requires extensive calculations. Depending on the purpose of the simulation, two domains in the weldment were selected in the present study. The first domain was selected as the dashed block shown in Fig. 10A to simulate real-time grain structure evolution in the HAZ around the weld pool. This domain covers the whole region of the HAZ where β grain growth occurs. The length, width and thickness of the simulation domain were 20 mm, 10 mm and 8 mm, respectively. A 400 x 200 x 160 grid system was used.

The second domain was selected as the thin dashed block shown in Fig.10B to focus on simulation of the final grain structure in the HAZ. The grid system used in this domain was 50 x 400 x 300, which corresponds the actual domain with the volume of 1.25 x 10 x 7.5 $mm^3$. Thus, the spacing of the grid points, 25 μm, was equal to the initial mean grain size. The initial β-Ti grain size, $L_0$, was assumed to be equal to the α-Ti grain size after recrystallization (25 μm). The grain size change due to the α→β transformation was not considered. Thus, the starting β-Ti grain size was set to an upper limit, since the grain size of the daughter phase is smaller than that of the parent phase. The selected domain was assumed to move at the same speed and in the same direction as the workpiece, as indicated in Fig. 10B.

#### Grain Growth Kinetics from MC Simulation under Isothermal Conditions

Before simulation of the grain growth under nonisothermal conditions, the dimensionless grain growth kinetics from the present MC model under isothermal conditions needs to be established. In other words, the values of $K_1$ and $n_1$ in Equation 18 need to be determined. Figure 11 shows the simulated isothermal dimensionless grain growth kinetics for the used two grid systems at 1548 K, which is the median of the melting temperature (1941 K) and the α→β transition temperature (1158 K). The data used for calculations are presented in Table 3. It can be observed the simulated grain growth kinetics in the two grid systems are actually the same. This is expected since the numbers of the grids in these two systems are very large and both systems use simple cubic grids. By geometric fitting of the data in Fig. 11, the values of the constants $K_1$ and $n_1$ in Equation 18 were determined to be 0.85 and 0.47, respectively.

#### Distributions of the $t_{MCS}$ and the Probability

After knowing the constants $K_1$ and $n_1$ of the present 3-D MC model, the $t_{MCS}$ at each site was calculated from Equation 21 by incorporating the corresponding thermal history into the equation. The distribution of the $t_{MCS}$ in the first domain using the 400 x 200 x 160 grid system is shown in Fig. 12A and B. From these figures, it can be observed that the maximum value of the $t_{MCS}$ lies at the locations nearest to the weld interface. The $t_{MCS}$ near the fusion zone change drastically due to the steep temperature gradient. This phenomenon is more evident at the edge in front of the weld pool. From Fig. 12A, it can also be observed the value of $t_{MCS}$ increases as the temperature or time for grain growth at a location increases. This can be easily understood by tracking a specific point in the domain as shown in Fig.12A. As the material at this location moves from point A to point B, the $t_{MCS}$ at this point will increase. After knowing the $t_{MCS}$ spatial distribution in the domain, the corresponding site selection probability, p(r), distribution can be obtained from

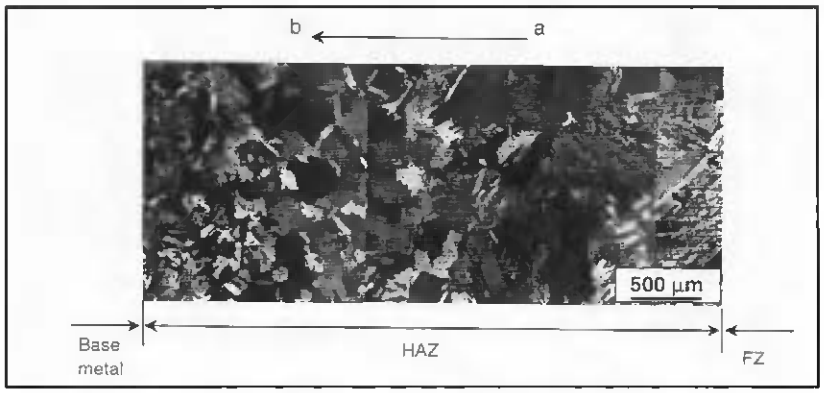


*Fig. 18 — Grain size gradient in the HAZ (50X). The direction indicated by line ab is labeled in Fig. 16.*

Equation 22, as shown in Fig. 13A and B. The spatial distribution of p(r) is similar to that of $t_{MCS}$.

Figures 14A and B show the distribution of the $t_{MCS}$ and p(r) in the domain shown in Fig. 10B using the 50 x 400 x 300 grid system. Compared to the values of $t_{MCS}$ in Fig. 14A and Fig. 12A, it can be observed the $t_{MCS}$ in the second grid system is much larger than in the first system. This is because the grid spacing in the second system is only half of that in the first grid system. The finer the grid system, the larger the $t_{MCS}$ needed for achieving the same grain size. After obtaining the p(r) distribution, the temperature time history at each site, as well as the material properties, can be incorporated into the model by considering the spatial site selection probability distribution in the simulation domain.

Simulated Grain Structure in the HAZ

After the introduction of the site selection probability into the MC model, the dynamic grain growth in the HAZ around the weld pool can be simulated. By using the first grid system, a real-time, three-dimensional map of grain structure distribution around the weld pool can be obtained, as shown in Fig. 15A, B, C. From these figures, the detailed grain structure in every location in the whole HAZ around the weld pool can be obtained. The grain structure at any plane in the domain can be viewed by examining any cross section. Furthermore, the real-time grain structure map can provide insight into the thermal and topological effects experienced in the HAZ. In the region in front of the weld pool, the grain growth is not significant and the grain size is fine due to the very short time for grain growth before the material at these locations melts. At the locations where the material does not melt, the mean grain size becomes coarser with time. In the meantime, the width of the HAZ increases with time. These features can be seen clearly in both the top and side views of the simulated grain structure map shown in Fig. 15B and C. The results shown here can provide detailed insight about the grain structure evolution under steep temperature gradient in the HAZ, which cannot be obtained otherwise.

The simulated final grain structure of the HAZ after the welding is completed is shown in Fig. 16. Significant spatial grain size gradient is observed in the simulated HAZ structure. The closer a site to the weld interface, the coarser the grain at that site. This is expected since the grain size change depends on both the temperature and the time period for grain growth. The higher the temperature and the longer the time for grain growth, the larger the final grain size. Furthermore, it can be observed grain growth on the top surface of the HAZ (along line ab) is not as significant as in the vertical direction shown by line cd in Fig. 16. This is because the temperature gradient on the top surface is relatively steeper and the time for grain growth is less than those at the bottom of the HAZ.

Along line ab on the top surface in Fig. 16, the calculated grain size gradient is compared with the experimental results in Fig. 17. It can be observed the calculated and the experimental grain sizes are comparable. The experimental grain size measurement was made after cooling to ambient temperature. Note that the grain size in the postweld microstructure is not the same as predicted in the single β phase region due to β→α transformation occurring during the cooling of the weldment. However, the prior β grain boundary can still be identified from the postweld microstructure, as shown in Fig. 18.

## Summary and Conclusions

The research reported here represents the first modeling of macro and microstructural features in GTA titanium weldments based on a combination of both rigorous transport phenomena and phase transformation theory. The modeling results were compared with the real-time phase mapping data in a region surrounding the liquid weld pool obtained using a unique 5RXRD technique with synchrotron radiation. Through the comparison of the calculated and experimental results, the conclusions below can be made.

1) The high-computed values of turbulent viscosity and thermal conductivity indicated the transport of heat and momentum in the weld pool was significantly aided by turbulence. Thus, previous calculations of heat transfer and fluid flow based on the assumption of laminar flow need to be re-examined. The geometry of the fusion zone, the α/(α+β) phase boundary and the β/liquid phase boundary predicted from the comprehensive 3-D turbulent heat transfer and fluid flow model were in good agreement with the experimental results.

2) The mechanism of the α→β transition was examined by the comparison of the calculated reaction times from several possible mechanisms with the experimentally determined reaction times. It was found the α→β transition was most likely controlled by the transport of Ti atoms across the α/β interface. The (α+β)/β phase boundary predicted from the combination of the calculated thermal cycles and the modified JMA equation agreed well with that determined from the experimental phase distribution map.

3) A real-time 3-D map of grain structure distribution around the weld pool was calculated by coupling the 3-D MC model with the calculated thermal cycles from the 3-D heat transfer and fluid flow model. This simulated real-time 3-D grain structure map can provide detailed insight into the dynamic grain structure evolution under steep temperature gradient in the HAZ that cannot be obtained otherwise. The simulated grain size distribution in the HAZ agrees well with the experimental results.

The above agreements between the calculated and experimental results indicate significant promise for understanding both macro and microstructures of titanium welds from the combination of the fundamental principles from both transport phenomena and phase transformation theory. Neither experiments nor modeling alone could have provided the detailed insight about the real-time evolution of macro and microstructures.

*Acknowledgments*

The Pennsylvania State University portion of this research was supported by a grant from the U.S. Dept. of Energy, Office of Basic Energy Sciences, Div. of Materials Sciences, under grant number DE-FGO2-B4ER45158. The Lawrence Livermore National Laboratory (LLNL) portion of this research was performed under the auspices of the U.S. Dept. of Energy, Lawrence Livermore National Laboratory, under Contract No. W-7405-ENG-48. The authors would like to express their gratitude to Kershaw of LLNL for performing optical metallography.

*References*

1. Oreper, G. M., and Szekely, J. 1984. *J. Fluid Mechanics* 147: 53–79.

2. Kou, S., and Wang, Y. H. 1986. *Metall. Trans. A*, 17A: 2265–2270.

3. Choo, R. T. C., Szekely, J., and David, S. A. 1992. *Metall. Trans. B*, 23B: 371–384.

4. Chan, C., Mazumder, J., and Chen, M. M. 1984. *Metall. Trans. A* 15A: 2175–2184.

5. Mundra, K., DebRoy, T., and Kelkar, K. 1996. *Numerical Heat Transfer* 29: 115–129.

6. Pitscheneder, W., DebRoy, T., Mundra, K., and Ebner, R. 1996. *Welding Journal* 75(3): 71-s to 80-s.

7. Mundra, K., Blackburn, J. M., and DebRoy, T. 1997. *Science and Technology of Welding and Joining* 2(4): 174–184.

8. Block-Bolten, A., and Eager, T. W. 1984. *Metall. Trans. B* 15B: 461–469.

9. Khan, P. A. A., and DebRoy, T. 1984. *Metall. Trans. B* 15B: 641–644.

10. Mundra, K., DebRoy, T., Babu, S. S., and David, S. A. 1997. *Welding Journal* 76(4): 163-s to 171-s.

11. Yang, Z., and DebRoy, T. 1997. *Science*

*and Technology of Welding and Joining* 2(2): 53–58.

12. Yang, Z., and DebRoy, T. Modeling Macro and Microstructures of Gas Metal Arc Welded HSLA-100 Steel, accepted for publication in *Metall. and Mater. Trans. B.*

13. Hong, T., Pitscheneder, W., and DebRoy, T. 1998. *Science and Technology of Welding and Joining* 3(1): 33–41.

14. Gedeon, S. A., and Eagar, T. W. 1990. *Welding Journal* 69(7): 264-s to 217-s.

15. Mundra, K., Blackburn, J. M., and DebRoy, T. 1997. *Science and Technology of Welding and Joining* 2(4): 174–184.

16. Palmer, T. A., and DebRoy, T. 1998. *Science and Technology of Welding and Joining* 3(4): 190–203.

17. Malinowski-Brodnicka, M., denOuden, G., and Vink, W. J. P. 1990. *Welding Journal* 69 (2): 52-s to 59-s.

18. Choo, R. T. C., and Szekely, J. 1994. *Welding Journal* 73(2): 25-s to 31-s.

19. Hong, K., Weckman, D. C., and Strong, A. B. 1996. *Trends in Welding Research,* eds. H. B. Smartt, J. A. Johnson and S. A. David, pp. 399–404. ASM International, Materials Park, Ohio.

20. Elmer, J. W., Wong, J., and Ressler, T. 1998. *Metall. Mater. Trans. A* 29A(11): 2761–2773.

21. Elmer, J. W., Wong, J., Fröba, M., Waide, P. A., and Larson, E. M. 1996. *Metall. Mater. Trans. A* 27A, : 775.

22. Wong, J., Fröba, M., Elmer, J. W. , and Waide, P. A. 1997. *J. Mater. Sci.* 32: 1493.

23. Ressler, T., Wong, J., and Elmer, J. W. 1998. *J. Phys. Chem.*, Vol. 102, 12/10 issue.

24. Kruger, P. 1993. *J. Phys. Chem. Solids* 54(11): 1549.

25. Anderson, M. P., Srolovitz, D. J., Grest, G. S., and Sahni, P. S. 1984. *Acta Metall.* 32: 783–791.

26. Srolovitz, D. J., Anderson, M. P., Sahni, P. S., and Grest, G. S. 1984. *Acta Metall.* 32: 793–802.

27. Saito, Y., and Enomoto, M. 1992. *ISIJ International* 32: 267–274.

28. Gao, J., and Thompson, R. G. 1996. *Acta Metall.* 44: 4565–4570.

29. Wilson, A., Martukanitz, R. P., and Howell, P. 1998. Experimental and computer simulation of grain growth in HSLA-100/80 steels during welding and cladding. To be published in the *5th International Conference on Trends in Welding Research.* Pine Mountain, Ga.

30. Burke, J. E., and Turnbull, D. 1952. *Prog. Met. Phys.* 3: 220.

31. Karpenko, V., Kinney, J. H., Kulkarni, S., Neufeld, K., Poppe, C., Tirsell, K. G., Wong, J., Cerino, J.,Troxel, T., Yang, J., Hoyer, E., Green, M., Humpries, D., Marks, S., and Plate, D. 1989. *Rev. Sci. Instrum.* 60: 1451–1460.

32. *Annual Book of ASTM Standards.* 1996. Vol. 1, Sect. 3. ASTM, West Conshohoken, Pa.

33. Launder, B. E., and Spalding, B. D. 1972. *Mathematical Models of Turbulence.* Academic Press, New York, N.Y.

34. Patankar, V. 1980. *Numerical Heat Transfer and Fluid Flow.* Hemisphere Publishing Corp., New York, N.Y.

35. Cormier, M., and Claisse, F. 1974. *J. Less-Common Metals* 34: 181.

36. Plichta, M. R., Aaronson, H. L., and Perepezko, J. H. 1978. *Acta Metallurgica,* 26: 1293–1305.

37. Massalski, T. B. 1970. *Phase Transformations,* pp. 433–486. ASM International, Materials Park, Ohio.

38. Ruch, M., and Arias, D. 1990. *Scripta Metallurgica et Materialia* 24: 1577–1582.

39. Johnson, W. A., and Mehl, R. F. 1939. *Trans. Am. Inst. Min. Engs.* 135: 416.

40. Avrami, M. 1941. *J. Chem Phys.*, 9: 177.

41. Christian, J. W. 1965. *The Theory of Transformations in Metals and Alloys,* Edition 1, Part I, Part XII and Part XV. Pergamon, Oxford, U.K.

42. Henderson, D. W. 1979. *J. Non-Cryst. Sol.* 30: 301.

43. Porter, D. A., and Easterling, K. E. 1992. *Phase Transformation in Metals and Alloys,* Chapman & Hall.

44. De Reca, N. E. W., and Libanati, C. M. 1968. *Acta Metall.* 16: 1297.

45. Murr, L. E. 1975. *Interfacial Phenomena in Metals and Alloys.* Addison-Wesley.

46. *Titanium Alloys.* 1994. ASM International, Materials Park, Ohio.

47. Radhakkrishnan, B., and Zacharia, T. 1995. *Metall. Mater. Trans. A* 26A: 167–180.

48. Song, X., and Liu, G. *Scripta Materialia* 38: 1691–1696.

49. Ignatov, D. V., Model, M. S., Sokyriansky, L. F., and Shinyaev, A. Ya. 1973. *Titanium Science and Technology,* Vol. 4, eds. R. I. Jaffee and H. M. Burte, p. 2535 Plenum Press, New York, N.Y.

50. Sahoo, P., DebRoy, T., and McNallan, M. J. 1988. *Metall. Trans. B* 19B: 483–491.

51. Lin, M. L., and Eagar, T. W. 1986. *Advances in Welding Science and Technology,* ed. S. A. David, pp. 47–51. ASM International, Materials Park, Ohio.

52. Gill, F. X., Rodriguez, D., and Planell, J. A. 1995. *Scripta Metallurgica et Materialia* 33: 1361–1366.

# Appendix

The grain boundary energies of metals are often found to be roughly ½ of their surface free energies (Ref. 43). The surface free energy of titanium is not available in the literature. However, the surface free energies of metals are related with their melting points. The higher the melting point, the higher the value of surface free energy (Ref. 43). This correlation can be seen in Fig. 19, which is drawn based on the data available in the literature (Ref. 45). By linear fit of the data in Fig. 19, the surface free energy of titanium can be estimated to be about 2.25 J/m$^2$. If the grain boundary energy of titanium is taken as ½ of this estimated surface free energy, its corresponding value will be 0.75 J/m$^2$. This estimated grain boundary energy is comparable with those of other metals whose melting points are close to titanium and experimentally measured value are available in the literature. For example, the grain boundary energy (Ref. 45) of γ-Fe is 0.756 J/m$^2$.

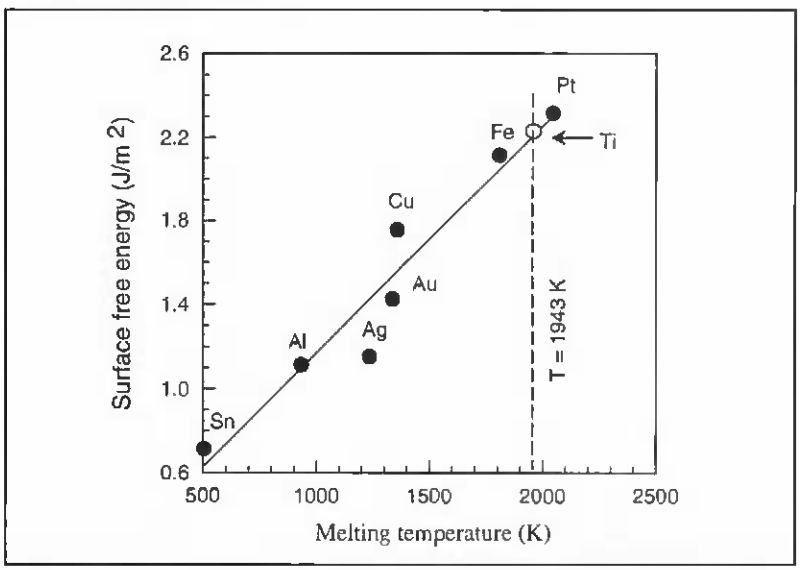


*Fig. 19 — Estimation of the surface-free energy of titanium based on the data of other metals available in literature (Ref. 44).*

## Nomenclature

| | |
|---|---|
| A | Accommodation probability for the jumping atoms |
| $C_1$,$C_2$,C | Empirical constants in K~ε model |
| $C_p$ | Specific heat, (J/kg-K) |
| f | Volume fraction of transformed phase |
| g | Acceleration of gravity, (m/s$^2$) |
| $G_K$ | Cartesian tensor notation in K ~ ε model, (s$^{-2}$) |
| ΔG(T) | Total activation energy for nucleation and growth, (J/mol) |
| h | Enthalpy, (J/kg) |
| $h_c$ | Heat transfer coefficient, (J/m$^2$-s-K) |
| $h_p$ | Planck's constant, (J/s) |
| $J_h(\xi,y,z)_{z=0}$ | Heat flux change on top surface, (J/m$^2$-s) |
| k | Molecular value of thermal conductivity, (J/m-s-K) |
| $k_B$ | Boltzmann constant, (J/K) |
| $k_{eff}$ | Effective thermal conductivity, (J/m-s-K) |
| $k_t$ | Turbulent thermal conductivity, (J/m-s-K) |
| $k_0$ | Pre-exponential constant in JMA equation |
| k(T) | Temperature-dependent kinetic constant in JMA equation |
| K | Turbulent kinetic energy, (m$^2$/s$^2$) |
| $K_1$ | Grain growth kinetic constant from MC simulation |
| $K_2$ | Pre-exponential constant for calculation of grain size |
| L | Average grain size at time t, (μm) |
| $L_0$ | Initial average grain size, (μm) |
| n | Kinetic constant in JMA equation |
| $n_1$ | Grain growth kinetic constant from MC simulation |
| $N_a$ | Avagadro's number, (mol$^{-1}$) |
| P | Effective pressure, (N/m$^2$) |
| $Pr_t$ | Turbulent Prandtl number |
| p(r) | Site selection probability in MC simulation |
| q | Welding power input, (J/s) |
| Q | Activation energy for grain growth, (J/mol) |
| $r_b$ | Radius of the arc beam, (m) |
| R | Gas constant, (J/mol-K) |
| $S_h$ | Heat source term considering heat input from welding source and heat loss by convection and radiation, (J/s-m$^2$) |
| $S_l$ | Heat source term considering latent heat of melting and convective transport of latent heat, (J/s-m$^2$) |
| $S_v$ | Momentum source term considering the combined effect of buoyancy force, Marangoni stress and electro magnetic force, (N/m$^3$) |
| $\Delta S_a$ | Activation entropy for grain growth, (J/mol-K) |
| t | Time, (s) |
| $t_0$ | Initial time of phase transformation, (s) |
| $t_{MCS}$ | MC simulation step or MC simulation time |
| $t_{MCS}^{max}$ | Maximum MC simulation step in the computation domain |
| Δt | Time increment, (s) |
| T | Absolute temperature, (K) |
| $T_s(\xi,y,z)$ | Temperature at coordinate (ξ,y,z) in steady-state temperature field, (K) |
| $T(\xi,y,z)_{z=0}$ | Local weld pool surface temperature, (K) |
| T(x,y,z,t) | Temperature at coordinate (x,y,z) at time t, (K) |
| $T_g$ | Ambient temperature, (K) |
| $T_0$ | Initial temperature of phase transformation, (K) |
| ΔT | Temperature increment, (K) |
| $V_x$,$V_y$,$V_z$ | Velocity components in the x, y and z directions respectively, (m/s) |
| V' | Transformed velocity, (m/s) |
| V | Convective component of the velocity, (m/s) |
| $V_m$ | Atomic molar volume (m$^3$/mol) |
| $V_s$ | Welding velocity, (m/s) |
| Z | Average number of atoms per unit area at grain boundary, (atoms/m$^2$) |
| ε | Dissipation rate of turbulent kinetic energy, (m$^2$/s$^3$) |
| $\varepsilon_1$ | Emissivity |
| γ | Surface tension of liquid metal, (N/m) |
| $\gamma_b$ | Grain boundary energy, (N/m$^2$) |
| η | Welding process efficiency |
| λ | Discrete grid point spacing in MC simulation, (μm) |
| μ | Molecular value of viscosity,(kg/m-s) |
| $\mu_{eff}$ | Effective viscosity, (kg/m-s) |
| $\mu_t$ | Turbulent viscosity, (kg/m-s) |
| ρ | Density, (kg/m$^3$) |
| σ | Stefan-Boltzmann constant, (W/m$^2$-K$^4$) |
| $\sigma_k$, $\sigma_e$ | Empirical constants in K–ε model |
| $\xi_1$, $\xi_2$ | Coordinates in x direction at time $t_1$ and $t_2$ respectively, (m) |